Influence of quantum defects on recurrence strengths of closed orbits

M. L. Keeler
Physics Department, University of Minnesota, Morris, Minnesota 56267, USA
(Received 4 September 2007; published 20 November 2007)

Experimentally obtained Stark-recurrence spectra taken at low principal quantum numbers show unusual degrees of *orbit profile asymmetry*. To clearly illustrate the semiclassical mechanisms behind this behavior a numerical experiment is performed where orbit profiles (recurrence strength as a function of scaled energy) are found from computed Stark spectra. These spectra are generated for a wide range of quantum defects assuming a highly simplified excitation and core structure which represents a semiclassical system restricted to *s*-wave scattering. It is noted that at low quantum numbers, the expected dominant nonhydrogenic feature of recurrence spectra is scattered orbits whose scaled actions are unresolved from existing hydrogenic orbits. The semiclassical orbit profiles obtained from absorption spectra are compared with semiclassical closed-orbit theory. Closed-orbit theory successfully predicts the systematic shifting of recurrence strength as a function of quantum defect. In the limited parameter space investigated it is found that the distribution of recurrence strength is influenced primarily by interference with scattered combinations containing a primitive orbit repetition. The systematic shifting of recurrence strength as a function of quantum defect is attributed to a relative phase shift between the contributing orbits.

DOI: 10.1103/PhysRevA.76.052510 PACS number(s): 32.30.−r, 32.60.+i, 32.70.Cs

I. INTRODUCTION

In this paper closed-orbit probabilities (recurrence strengths) for orbits within a nonhydrogenic Stark system are computed numerically using two distinct methods. One is a direct computation using semiclassical closed-orbit theory; the other involves identifying recurrences, which can be correlated with closed orbits, from a computed Stark spectrum. Significant portions of this paper are devoted to a review of the basic concepts and practical considerations of computing recurrence spectra. These two distinct computations are then compared with one another to identify the semiclassical mechanism behind observed asymmetries in the recurrence strength along orbit profiles (orbit probability as a function of scaled energy). Beyond interpreting the specific observed asymmetries in experimental argon and helium data, these computations are performed over a wide range of quantum defect parameters (a measure of core influence), allowing for a more general semiclassical interpretation of the quantum defect.

Closed-orbit theory (COT) asserts that the spectral features of a highly excited atomic system are dictated by the classical trajectories, originally launched from the core that return and close at the core. COT is semiclassical, and the computed recurrence strength includes effects of wave interference between classical trajectories that neighbor one another in classical action. In atomic systems, the core region must be treated quantum mechanically, so the complete theory includes the opportunity for wavelike behavior near the core. In the absence of any quantum mechanical influences the recurrence strength represents the classical orbit stability [1].

In practice, an experimentally observed spectrum may be taken under conditions of classical scaling. Sinusoidal oscillations within the observed spectrum are then extracted via a Fourier transform and directly interpreted as recurrence strengths. This technique of obtaining scaled absorption spectra and translating them into semiclassical recurrence strengths is known as recurrence spectroscopy [2,3]. The final result is an interpretation of absorption spectra in terms of a coherent collection of classical orbits. (It is tempting to interpret recurrence spectra classically, but this interpretation is oversimplified because recurrence strengths include nonclassical influences.)

Presented here are recurrence spectra for the nonhydrogenic Stark system generated from quantum-computed absorption spectra and primitive closed-orbit theory. Recurrence spectra found from computed absorption spectra reproduce the asymmetric recurrence strengths seen in experimental argon data, and this asymmetry was directly linked to an asymmetry in the absorption spectra [4]. More generally, if the quantum defect is treated as a continuous variable, as it is increased from zero, the oscillator strength distribution across the Stark manifold cycles from symmetric (integer defects) to asymmetric (noninteger defects) and back again. Similar to the interpretation of the argon spectra, the cyclic shift of oscillator strength in Stark spectra as a function of quantum defects can be directly associated with a cyclic shift in recurrence strength. The recurrence strengths extracted from computed absorption spectra in this paper, as expected, demonstrate the cyclic shifting of recurrence strength as a function of quantum defects. To provide a semiclassical interpretation, these computations are then compared with semiclassical closed-orbit theory calculations. In this analysis classical orbits are added as necessary to recreate the observed recurrence patterns. While the collection of core-scattered orbits may be complex, it is found that combination orbits involving a single-scattering event with a primitive parallel-orbit repetition are responsible for the shifting recurrence strengths. The interference of the hydrogenic orbit with the collection of nonhydrogenic combination orbits is what generates the observed systematic shifting of recurrence strength within orbit profiles.

II. STARK OSCILLATOR STRENGTHS

The technique of recurrence spectroscopy allows one to take spectroscopic data, obtained experimentally or via quantum calculations, and turn them into recurrence spectra, thereby allowing for a semiclassical interpretation of quantum spectra. Absorption spectra based on quantum mechanical computations are more flexible than their experimental counterparts, and specific atomic and excitation parameters have been selected to simplify the subsequent semiclassical interpretation. Because nature has provided us with a discrete set of atoms, each with an entire *set* of quantum defects, direct correlations between the quantum defect parameter and recurrence strength are not easily demonstrated with calculations for the alkali-metal series. To obtain a clearer understanding of inner-core influences on a highly excited Stark state, quantum calculations were performed on atomic systems with assigned *s*-quantum defects (δ_s) ranging from 0 to 2. The higher-angular-momentum defects ($\delta_p, \delta_d, \delta_f, \ldots$) were set to zero, implying that semiclassically all core scattering can be interpreted as *s*-wave scattering. Experimental excitation of Rydberg states is commonly restricted to *s*-*p* transitions or, even less desirable, some combination of *p*-*s* and *p*-*d* transitions. The classical interpretation of such transitions is the simultaneous launch of trajectories with an initial angular distribution described by the spherical harmonic function $Y_{lm}(\theta,\varphi)$ [5]. An absorption spectrum computed for a *p*-*s* transition is then understood to represent a uniform launching distribution $Y_{00}(\theta,\varphi)$, eliminating the need to consider the initial launching angle probabilities when interpreting recurrence spectra.

All Stark spectra were calculated using the matrix diagonalization technique described by Zimmerman *et al.* [6]. Further details of the calculation method can be found in Appendix A. The basis set consisted of all zero-field atomic states within the $n=17-34$ manifolds. Figures 1(a) and 1(b) show the results of the calculation for $\delta_s=0.2$ and $\delta_s=0.8$ in the vicinity of the $n=20-21$ manifolds. The oscillator strengths, represented by grayscale, are calculated for a transition into an $s,m=0$ state. Thus the intensity scale is also a distribution map of the "*s* character" within the manifold. At zero field all the oscillator strength is contained within the nondegenerate *s* state. As the external electric field strength is increased the *s* state mixes with the rest of the manifold, redistributing the oscillator strength. In general, for a quantum defect whose modulus is less than 0.5 the oscillator strength is preferentially distributed to the nearest redshifted Stark states. Conversely, when the modulus of the quantum defect is greater than 0.5 the oscillator strength of the emerging *s* state is mixed into the neighboring blueshifted Stark states.

III. COMPUTING RECURRENCE SPECTRA FROM ABSORPTION SPECTRA

In the Stark system, the classical Hamiltonian

$$H=\frac{p^2}{2}-\frac{1}{r}+Fz, \tag{1}$$

where z is parallel to the direction of the external electric field and F is the field strength (atomic units), can be transformed to a set of scaled coordinates $\tilde{r}$, $\tilde{p}$, and $\tilde{z}$ defined as

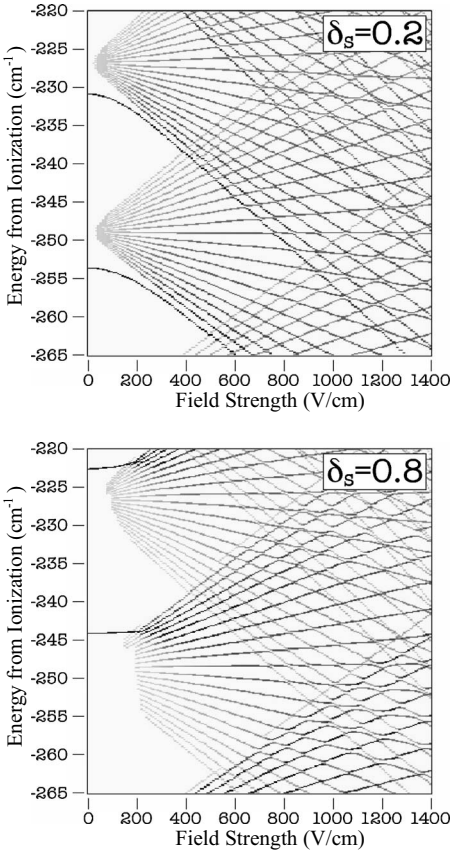

FIG. 1. Stark maps in the vicinity of $n=21-22$ for a quantum defects of 0.2 and 0.8. Grayscale covers two decades of oscillator strength.

$$r=F^{-1/2}\tilde{r}, \quad p=F^{1/4}\tilde{p}, \quad z=F^{-1/2}\tilde{z}. \tag{2}$$

The Hamiltonian, rewritten in terms of the scaled coordinates, becomes $\tilde{H}=\frac{\tilde{p}}{2}-\frac{1}{\tilde{r}}+\tilde{z}$ or $\tilde{H}=H/\sqrt{F}$, suggesting a scaled energy

$$\varepsilon=E/\sqrt{F}, \tag{3}$$

where E is the energy of the excited electron from ionization [5]. If the scaled energy is maintained as a constant, then the *scaled* Hamiltonian is independent of the external field strength and the classical dynamics remains unchanged. The energy of the excited electron can be increased as long as the external field is modified to maintain a constant scaled energy. In doing this, the electron orbit becomes larger, but the classical dynamics remains unchanged, so in effect the classical orbits are expanding in size. As an electron, launched from the core, returns, it is capable of interfering with itself. The probability of absorption of the photon that leads to excitation is dependent on this interference. The constructive or destructive nature of the interference, and ultimately the photon absorption probability, is dependent on the phase of the returning electron. To first order the phase can be determined by the WKB approximation and the classical action *S*,

$$\phi = \frac{1}{\hbar}\oint pdl = \frac{1}{\hbar}S, \tag{4}$$

and in scaled coordinates the final oscillator strength density contribution from a single closed orbit $Df(\varepsilon, F^{-1/4})$ can be written

$$Df(\varepsilon, F^{-1/4}) = C_k(\varepsilon)\sin\left(\frac{2\pi}{\hbar}\tilde{S}(\varepsilon)F^{-1/4} - \alpha\right), \tag{5}$$

where C_k is the recurrence amplitude of the orbit, $\tilde{S}$ is the scaled action ($S=\tilde{S}n_{avg}\sqrt{-2\varepsilon}$), and α is a phase factor that takes into account the effects of a nonhydrogenic core and caustics. If an absorption spectrum is obtained under conditions of constant ε (scanning both E and F appropriately), a single closed orbit (expanding in size) will contribute a sinusoidal variation in the absorption spectrum with respect to $F^{-1/4}$, a parameter also known as w. Because the initial excitation is quantum mechanical in nature, electrons are launched simultaneously in all directions (in our case, because of the p-s transition, all directions contribute with equal probability) and every one of these closed orbits contributes a sinusoidal variation to the final absorption spectrum. To extract the amplitude coefficients (C_k) from the data, a scaled absorption spectrum is taken along a line of constant scaled energy ε and then interpolated with data points spaced equally with respect to the parameter w. Taking the power spectrum of the scaled absorption spectra generates a recurrence spectrum whose x axis is the scaled action and y axis is the recurrence strength (proportional to C_k^2),

$$(C_{m,k,n})^2 \propto A_k^2 \tilde{y}_m(\theta_f^{m,k})\tilde{y}_m(\theta_i^{m,k})(\sin\theta_i^{m,k}\sin\theta_f^{m,k}), \tag{6}$$

and in the case of an s-state excitation the launching angle probability distribution $\tilde{y}_m(\theta)$ reduces to a constant. The square of the classical amplitude, A^2, referred to as the classical stability, can also be found from the two-dimensional Jacobian, where

$$A_j(t) = \frac{1}{\sqrt{J(t)}}, \quad J(t) = \begin{vmatrix} \frac{dr}{dt} & \frac{d\theta}{dt} \\ \frac{dr}{d\theta_i} & \frac{d\theta}{d\theta_i} \end{vmatrix}. \tag{7}$$

For closed-orbit theory, the Jacobian and classical amplitude need only be calculated upon return to the core, not along the entire path [5,7]. Peaks in the recurrence spectrum can be correlated with classical trajectories, where the recurrence strength is directly proportional to the classical stability. Classical calculations are then used to identify the scaled action locations of specific closed orbits. Figures 2(a)–2(c) show the recurrence *maps* generated from hydrogen ($\delta_s=0$) and the Stark spectra in Figs. 1(a) and 1(b), respectively. The recurrence map is a series of recurrence spectra displayed as a function of the scaled energy parameter ε. In the recurrence maps of Fig. 2, the grayscale represents the recurrence strength. Orbits are typically identified by the number of oscillations in hyperbolic coordinates (u,v), which are adapted to aid in solving the equations of motion (Appendix C).

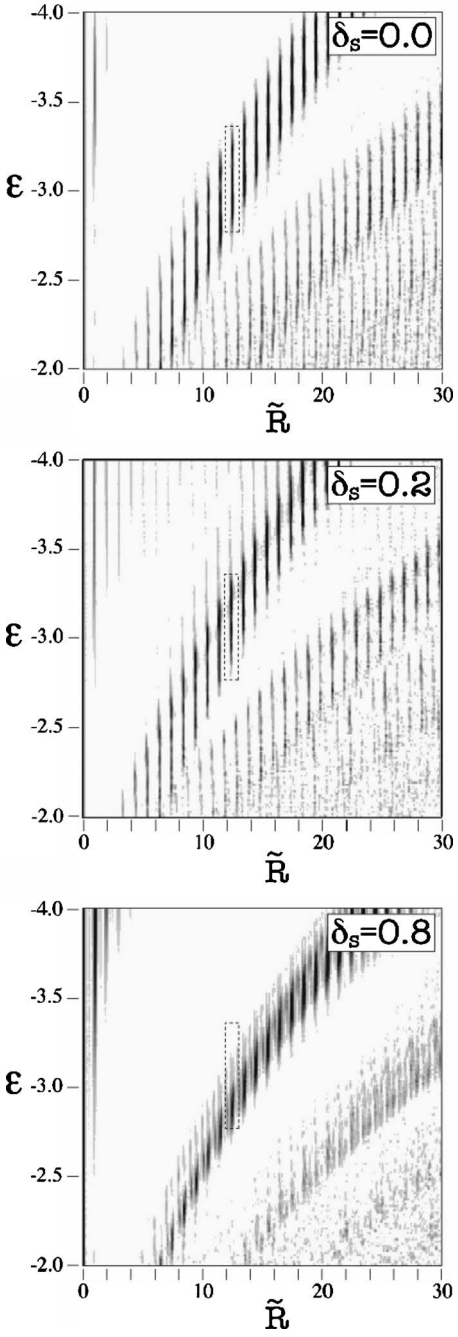

FIG. 2. Recurrence maps generated from hydrogen Stark map in the $n=20-30$ range and for quantum defects $\delta=0$, 0.2, and 0.8, respectively. Grayscale represents the recurrence strength. The dotted box represents the area around the classically identified 12/13 period ratio orbit and occurs at $\tilde{R}\cong 12.5$.

To simplify orbit identification the scaled action ($\tilde{S}$) for each recurrence spectra has been stretched (multiplied) by a factor of $\sqrt{-2\varepsilon}$. This stretch causes all orbits with a constant period ratio (motion along u and v hyperbolic coordinates) to lie on approximately vertical lines [8]. To avoid using the term "scaled-scaled action" I will refer to this stretched scale as the scaled ratio $\tilde{R}$.

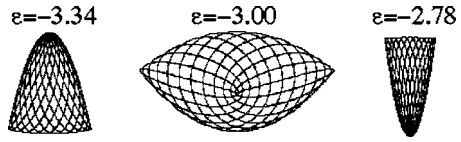

FIG. 3. Classical trajectories of the 12/13 period ratio orbit at different ε. The force exerted on the orbiting electron by the external electric field is pointing down.

IV. GENERAL OBSERVATIONS OF RECURRENCE MAPS

I will first summarize some of the previously noted structures visible in the recurrence maps of Fig. 2. Continuous groups of recurrence strength lying along vertical lines in the recurrence maps locate orbits of constant period ratio. In semiparabolic space, the equations of motion for hydrogen are separable and the period ratio is the ratio of u to v oscillations. We define the orbit profile as the recurrence strength versus scaled energy for an orbit with a given period ratio. This can be extracted from a recurrence map by integrating the strength over a small range of scaled action. An orbit with a constant period ratio reacts against the external field as the scaled energy is increased [8]. Figure 3 shows the trajectories for the 12/13 period ratio orbit for low ($\varepsilon=-3.34$), medium ($\varepsilon=-3$), and high ($\varepsilon=-2.78$) scaled energy. Notice that the number of orbital oscillations is 12 for the downhill-oriented orbit (electron moving with external field) and 13 for the uphill-oriented orbit (electron working against external field). For higher scaled energy, one reaches the classical bifurcation where the 12/13 orbit becomes the 13th repetition of the primitive uphill orbit. At lower scaled energy this same orbit reaches a bifurcation with the 12th repetition of the primitive downhill orbit. Assuming a uniform probability for all possible launching angles, the recurrence strength for a given orbit should be nearly symmetric with respect to the bifurcation boundaries.

In Fig. 2 the classical bifurcation limits of the 12/13 orbit are the upper and lower bounds of the small dotted region. As noted in a previous paper, recurrence strength exists beyond the classical region as a result of quantum tunneling not predicted in a pure classical model [9]. Recurrence maps also organize in band structures. The first obvious band (series of orbits running from lower left corner of map to upper right) is composed of orbits with a period ratio $i/(i+1)$. The second band is composed of orbits with period ratio $i/(i+2)$ and a less visible third band with period ratio $i/(i+3)$. Also visible in the second band of nonhydrogenic maps is a regular modulation of the recurrence strength as a function of orbit type [10,11]. Finally, several groups have identified core scattering as the mechanism that generates combination orbits at actions equal to the sum of two hydrogenic orbits [12–16]. Evidence of these combination recurrences are seen in the $\delta=0.8$ recurrence map as faint lines between the primary orbit locations in the first band.

V. CLASSICAL AMPLITUDE AND ORBIT PROFILE SYMMETRY

The recurrence strength is semiclassical and contains the effects of nonclassical behavior near the core in addition to the effects of classical stability of individual orbits. The quantum mechanical influences during the initial launching, because of our transition choice p-s, have been effectively eliminated. The recurrence strength variations observed along an orbit profile can now be reduced to the classical orbit stability and interference between orbits upon return to the core. For a single orbit the classical stability can be computed by integrating the equations of motion (Appendix C) and calculating the Jacobian. Plotting the square of the returning amplitude of an orbit with a specific period ratio as a function of launching angle (which can be directly related to the scaled energy ε) will return an orbit profile. Figure 4 shows a select region of a recurrence map for hydrogen generated from computed absorption spectra. The recurrence strength has been integrated from $\tilde{R}=8.25$ to 8.75 to generate the orbit profile to the right of the map. The square of the classical amplitude (thick gray line) deviates significantly from the spectrally derived recurrence strength. One difference is that the classical orbit stability approaches a singularity near the classical orbit bifurcations which occur at the scaled actions indicated by horizontal dotted lines. This artifact is explained if one accounts for diffraction of the retuning electron [17]. The other deviations between the profiles can be accounted for if one considers interference between the primary 8/9 orbit and nearby primitive orbit repetitions. The primitive uphill orbit is launched parallel to the external field and the downhill is initially launched antiparallel to the external field. The $u9$ and $d8$ primitive repetitions are close in action to the 8/9 orbit, thus contributing to the total strength coherently. The interference between these orbits causes oscillations along the orbit profile as a function of scaled energy. In the limit of high n, if the spectra are taken over a relatively large range of energies, the spectrally derived profile will approach the classical.

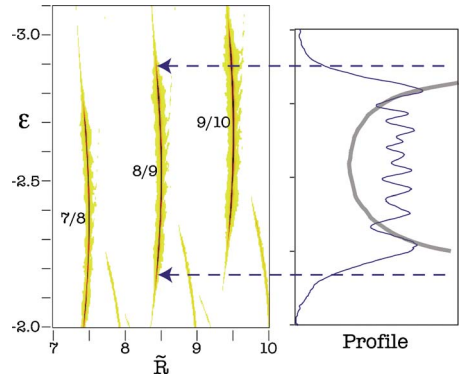

FIG. 4. (Color online) Left, recurrence map of hydrogen in the vicinity of the 8/9 orbit generated from the absorption spectra extending from the center of the $n=55$ to 65 manifolds. Right, orbit profile is the thin line (integrated strength from $R=8.25$ to 8.75), and the classical stability is shown as a thick gray line. The integrated recurrence strength scale (x axis) is in arbitrary units.

Both of the profiles shown in Fig. 4 are very nearly symmetric with respect to the classical bifurcation locations. Appendix B identifies and addresses two small contributors to orbit profile asymmetry in hydrogen, but thus far there have been no specific semiclassical mechanisms proposed that

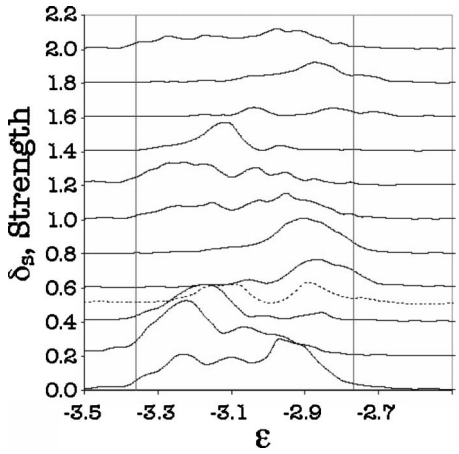

FIG. 5. 12/13 orbit profiles as a function of quantum defect obtained from computed Stark-spectra in the $n=20-30$ range. Vertical axis represents relative recurrence strength (arbitrary units), with the base line of each profile in line with the corresponding quantum defect. Vertical lines indicate the classical bifurcation locations for the 12/13 orbit.

would generate the degree of orbit profile asymmetry observed in experiment or the orbit profiles associated with Fig. 2. Orbit profiles were calculated for the 12/13 orbit from each of our computed recurrence maps. Each orbit profile was obtained by integrating the recurrence strength over the range $\tilde{R}=12.25-12.75$. With this we could observe the evolution of a single orbit profile as a function of quantum defect. Figure 5 shows the results of these calculations.

The extreme levels of orbit asymmetry seen in quantum defects 0.4, 0.8, 1.4, and 1.8 cannot be explained by classical stability computations of a single orbit or by artifacts of the finite range of basis functions used in the quantum calculation. Note the reduction in orbit strength when comparing quantum defects of 0, 1, and 2. This is presumably caused by the classical orbit strength being scattered into other orbits at higher actions [9].

VI. ORBIT SCATTERING MANIFESTED IN THE ABSORPTION SPECTRUM

The orbit profiles of Fig. 5 show systematic recurrence asymmetry along orbit profiles [4]. We can look for the source of this asymmetry in the absorption spectra itself. For nonhydrogenic atoms, the oscillator strength of Stark manifolds is asymmetric due to the lifted degeneracy at zero field and subsequent mixing of oscillator strength at higher fields. After performing a power spectrum on the scaled version of this manifold and obtaining a recurrence map, the asymmetry in oscillator strength can be directly correlated to an asymmetry in recurrence strength. In theory, if one were to start with hydrogen and increase the quantum defect as a continuous parameter, the asymmetry in oscillator strength across the Stark manifold would shift continuously back and forth from the redshifted states to the blueshifted. Subsequently, the recurrence strength in the region of a specific orbit type would be shifted back and forth from downhill to uphill character. This observation is important, but not surprising considering the mathematical relationship between an absorption spectrum and its corresponding recurrence spectrum. The shifting of strength within a recurrence map has been attributed to interference between orbits [10], but it is important to note that a shifting of oscillator strengths can only influence the distribution of recurrence strengths within a recurrence spectrum. Scattered orbits whose action occur at uniquely nonhydrogenic peak locations must originate from new spectral frequencies generated by avoided crossings. Both the oscillator strength distribution and avoided crossings play a role in the final distribution of recurrence strengths, but at low values of n, the distribution of oscillator strengths becomes the dominant nonhydrogenic feature of the spectrum. For example, the $n=11$ and 12 Stark manifolds do not cross and have no avoided crossings until the field reaches the classical ionization limit at $\varepsilon=-2$. In contrast, the $n=95$ and 98 manifolds cross through intermediate manifolds and make contact at much lower fields, around $\varepsilon=-5$. At very high quantum numbers, oscillator strength distributions found at low field strengths are quickly homogenized as overlapping manifolds mix. Thus, for high quantum numbers, state mixing reduces the impact of asymmetrically distributed oscillator strengths found at low fields and avoided crossings are the dominant nonhydrogenic feature of the spectrum. In these recurrence spectra, one would expect to find most scattered combination orbits at scaled actions not seen in hydrogen. For low quantum numbers, an asymmetric oscillator strength distribution can persist at even moderate field strengths and this becomes the dominant nonhydrogenic feature. This implies that the nonhydrogenic signatures of a recurrence map obtained from spectra at low quantum numbers will be a shifting of recurrence strength among peaks already found in hydrogen. In this case the new distribution of recurrence strength can be attributed to interference with scattered orbits whose actions are unresolved from the actions of hydrogenic orbits.

VII. ASYMMETRY IN ORBIT PROFILES AND PRIMITIVE CLOSED-ORBIT THEORY

A simple recurrence spectrum can be generated from integrating the equations of motion. Peaks, infinitely narrow, located at the scaled actions of closed orbits, have heights that are equal to the classical stability. But when trying to interpret recurrence strengths derived from absorption spectra over a finite range of energies, nonclassical effects in the region of the core become increasingly influential. In a single recurrence spectrum every orbit can potentially interfere with every other orbit; mathematically, this is realized by a sum of sinc functions in contrast with a sum of classical δ functions:

$$RS(\tilde{S}) = \left(\sum_k D_k \frac{\sin(a x_k)}{a x_k} \right)^2, \tag{8}$$

where

$$x_k = \tilde{S}_k - \tilde{S}, \quad a = \pi\sqrt{-2\varepsilon}(n_p - n_q), \tag{9}$$

and the index k identifies individual trajectories. The width of the sinc function is determined by the range (principal

quantum number range $n_p - n_q$) of the spectrum to be modeled. The effective half-width of individual orbit recurrences is

$$\Delta\tilde{S} = (\Delta n\sqrt{-2\varepsilon})^{-1} \tag{10}$$

or $\Delta\tilde{R} = \Delta n^{-1}$. In the limit of high n, where the density of states and spectral range are high, the sinc distribution approaches a classical δ function. For finite-width peaks the phase of the electrons returning to the core must be defined for every scaled action, and this phase is incorporated into the amplitude D_k:

$$D_k = C_k e^{i(b\tilde{S} - \Phi_k)}, \tag{11}$$

where

$$b = \pi\sqrt{2\varepsilon}(n_1 + n_2) \tag{12}$$

and ϕ_k represents an additional phase that carries contributions from classical turning points and the nonhydrogenic core. In terms of $\tilde{R}$, orbit recurrence strengths a distance $\Delta\tilde{R}$ from the central orbit action experience a phase shift of

$$\varphi = \pi\Delta\tilde{R}(n_1 + n_2). \tag{13}$$

In the limit of high n, the phase changes rapidly as a function of scaled action and its influence becomes unobservable. The phase contributions from classical turning points and quantum defects are detailed elsewhere [18] and can be reduced to

$$\Phi_k = 2\pi\delta - \pi\mu_k/2, \tag{14}$$

where μ_k is known as the Maslov index. In semiparabolic coordinates the Maslov index advances by 1 each time the orbit crosses the u or v axis, or at a classical focus. Each time the orbit crosses the origin μ_k is increased by 2. A computer code was written to search for closed orbits and record a list of scaled action, classical amplitude (C_k), and phase (ϕ_k). A second program uses that list to compute the recurrence spectra based on the summation of sinc functions. As a check, recurrence strengths for hydrogen were computed for the primitive repetitions and 12/13 orbit and compared with the spectrally derived strengths.

For hydrogen, the primitive repetitions $u13$ and $d12$ are in close proximity with the 12/13 period ratio orbit and the results of this can be seen in the first panel of Fig. 7. The $u13$ and $d12$ primitive repetitions pass through the core region 13 and 12 times, respectively, each time losing an additional $2\pi\delta$ in phase, whereas the 12/13 orbit experiences this additional phase shift only once. The resulting orbit profile, taking the interference between the primitive repetitions into account, still suffers from the classical singularity near the bifurcation points. To simulate the effects of diffraction the classical stability is convoluted with a Gaussian function. The half-width of the function, in this case $\Delta\varepsilon = 0.5$, is chosen to optimize the agreement with the spectrally derived computation. As the quantum defect is increased the relative phases between the primitive repetitions and the primary orbit shift, causing the interference to also shift. But because of the nearly symmetric placement of the primitive orbits with respect to the primary orbit, this interference, independent of the quantum defect, still produces nearly symmetric orbit profiles and cannot explain the recurrence strength variations seen in Figs. 2 and 5.

A nonhydrogenic core also leads to the possibility of core-scattered combination orbits. As a launched orbit returns to the core, scattering can occur into a completely different orbit, forming a combination orbit where the action of the newly formed orbit is the sum of the parent orbits and the recurrence amplitude is proportional to the product of the parent amplitudes:

$$\tilde{S}_{combination} = \tilde{S}_1 + \tilde{S}_2 \text{ and } C_{combination} = C_1 C_2 P(\delta), \tag{15}$$

with an additional π phase shift introduced [2].

Because the semiclassical theory is being used to model a system with s-quantum defects, the returning electron is scattered in all directions with equal probability. The classical amplitude of the combination is the product of the parent classical amplitudes multiplied by a scattering factor $P(\delta)$.

The 12/13 orbit was selected because of the limited possible contributions from combination orbits. The strongest combination orbits will necessarily originate from the strongest orbit recurrences, with multiple-scattering combinations being less probable. The strongest orbits lower in action than the 12/13 orbit are the preceding 11/12, 10/11, and 9/10 period ratio orbits. These can scatter and form combinations of orbits with repetitions of the primitive uphill and downhill orbits. The classical amplitude of the primitive repetitions is proportional to $1/\sqrt{j}$ where j is the number of repetitions. *The relative phase between a combination orbit and the primary orbit should be independent of the quantum defect, but because one of the combination orbit parents is a primitive repetition, the additional phase introduced by the core into the repetition is inherited by the combination orbit*. The relative phase between the primary and combination orbit will evolve with a changing quantum defect and can be written

$$\Delta\Phi = (j-1)\delta_s 2\pi. \tag{16}$$

Because this shift in phase is a continuous function of the quantum defect, the interference between the 12/13 and combination orbits also varies in a continuous way. In the vicinity of the 12/13 orbit, the 12th and 13th primitive uphill and downhill repetitions are weak when compared with scattered orbit combinations such as the 10/11 combined with a single primitive uphill repetition orbit (10/11+$u2$ orbit). The six strongest orbits which influence the measured 12/13 orbit profile are the 11/12+$u1$, 11/12+$d1$, 10/11+$u2$, 10/11 +$d2$, 9/10+$u3$, and 9/10+$d3$. These represent the few combinations of strong orbits that fall within reasonable range of the 12/13 orbit action. The combinations involving downhill repetitions fall at actions higher than the 12/13 orbit, and combinations with uphill repetitions are found at slightly lower actions. The combinations with primitive repetitions for one parent (such as 10/11+$u3$) fall further from the 12/13 in action and are slightly weaker due to the $1/\sqrt{j}$ dependence of the repetition amplitude (where j is the repetition number) [14]. Although the combinations involving a single primitive orbit are the strongest contributors (11/12

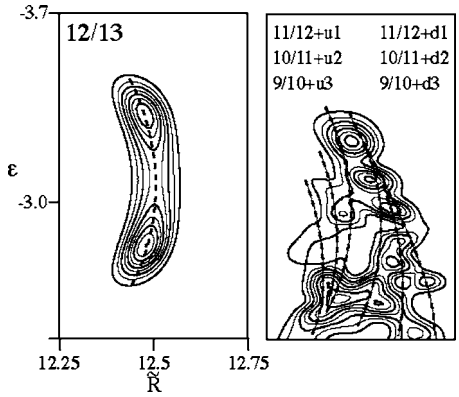

FIG. 6. Maps illustrating the contributions to recurrence strength in the vicinity of the 12/13 orbit. On the left is a contour plot of recurrence strength for the 12/13 orbit with a dotted line locating the classical action. On the right is the contour plot of recurrence strength for the six strongest scattered orbits. The classical orbit actions are indicated by dotted lines. The recurrence strength in this map represents the coherent addition of all six combination orbits (without the 12/13 orbit). Each map covers the same range of action and scaled energy with contours covering an order of magnitude in recurrence strength.

$+u1$, $11/12+d1$), because their phase *does not shift* with respect to the primary orbit as a function of quantum defect, they cannot be considered to be the source of shifting orbit recurrence strength (function of quantum defect). Figure 6 shows recurrence maps in close vicinity of the 12/13 orbit. These maps represent the recurrence strength using contours and were computed using primitive closed orbit theory. The map on the left was computed using just the isolated 12/13 orbit, whereas the map on the right includes, in *isolation*, only the neighboring combination orbits. The classical orbit actions are indicated by dotted lines. In the limit of high n, these orbits would remain distinct classical entities, but in the quantum range investigated ($n=20-30$) each orbit has a scaled action half-width of approximately $\Delta\tilde{R}=1/\Delta n=0.1$. The six orbits contributing to the graph on the right of Fig. 6 are *unresolved* as individual orbits and interfere to form the coherent structure shown. The final measured orbit profile along the 12/13 orbit (integrated strength from $\tilde{R}=12.25$ to 12.75) will consist of the coherent addition of these two graphs. As the quantum defect is changed the scattered orbits containing a primitive *repetition* will shift in phase with respect to the primary orbit.

Figure 7 shows the results from primitive closed-orbit theory for the coherent addition of all seven orbits as a function of quantum defect. The results qualitatively reflect the same regular shift in recurrence strength as the quantum calculations. The shift in strength is caused by interference with the combinations involving a primitive repetition ($10/11+u2$, $10/11+d2$, $9/10+u3$, $9/10+d3$). Multiple-scattering orbits such as $10/11+u1+d1$, $9/10+u2+d1$, and $9/10+d2+u1$ were introduced without qualitatively changing the shifting of recurrence strengths as a function of quantum defect.

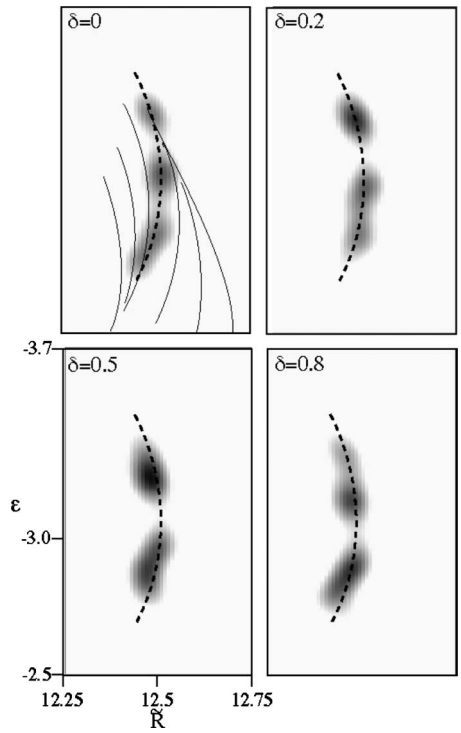

FIG. 7. COT-derived recurrence maps in the vicinity of the 12/13 orbit for different quantum defects. Each map covers the range $\varepsilon=-3.7-2.5$ and $\tilde{R}=12.25-12.75$, with the recurrence strength indicated by a grayscale. As the quantum defect is increased combination orbits shift in action and phase with respect to the main orbit producing a shifting in recurrence strength across the orbit profile.

VIII. SUMMARY

For low fields and low quantum number ranges, specifically $n=20-30$ and $\varepsilon<-2.7$, the oscillator strength across the Stark manifold shifts between blue and red as a function of quantum defect. Investigating this distribution of oscillator strengths using recurrence spectroscopy techniques it is found that a corresponding shift in recurrence strengths between downhill- and uphill-oriented orbits also occurs. Small asymmetries in orbit profiles are generated in spectrally derived recurrence maps due to the use of a finite basis, but this alone does not explain the observed asymmetries in nonhydrogenic orbit profiles. Using primitive closed-orbit theory it is found that the effective recurrence strength as a function of scaled energy (orbit profile) is strongly influenced by interference of a primary orbit with scattered combination orbits. Because the combination orbits contain repetitions of the uphill and downhill orbits, the relative phase of the combination orbits with respect to the main orbit is dependent on the quantum defect. The collective interference evolves as a function of quantum defect to reproduce the observed asymmetries in computed recurrence maps. This mechanism is consistent with the idea that with low quantum numbers, oscillator strength distributions are the dominant nonhydrogenic spectral feature and these can be correlated with scattered orbits which occur at actions indistinguishable from hydrogenic orbits.

ACKNOWLEDGMENT

I wish to acknowledge and thank John Delos for his patient discussions and comments on this paper.

APPENDIX A: CALCULATION OF STARK ABSORPTION SPECTRA

Details of this calculation can be found in Reference [19]. The Stark absorption spectra were obtained using matrix diagonalization, the basis set being the field-free nonhydrogenic wave functions. The wave equation can be separated into radial and angular components, where the solution to the angular equation is the same as that in hydrogen. Substitutions to the radial wave equation

$$\frac{\partial^2 R}{\partial r^2} + \frac{2}{r}\frac{\partial R}{\partial r} + \left[2W + \frac{2}{r} - \frac{l(l+1)}{r^2}\right]R = 0, \tag{A1}$$

where W represents the known eigenvalues,

$$W = -(n-\delta_l)^{-2}/2, \tag{A2}$$

can be made to generate an equation of the form that is easily solved using the Numerov algorithm. Making the substitutions $x=\ln(r)$ and $Y(x)=R\sqrt{r}$ transforms the wave equation into

$$\frac{d^2 Y}{dx^2} = g(x)Y(x), \tag{A3}$$

where

$$g(x) = 2e^{2x}\left(-\frac{1}{r} - W\right) + \left(l+\frac{1}{2}\right)^2,$$

and this equation is integrated inward from large distances, where $Y(x)$ is small. A square Hamiltonian matrix is computed, consisting of all the n,l states from $n=17-34$, measuring 460 cells on a side. With each element the external field is considered as a small perturbation $\langle nlm|z\Delta F + H_0|n'l'm'\rangle$. This matrix, once diagonalized, returns a new set of eigenvalues and eigenvectors, W,l,m, each of which is a linear combination of n,l,m nonhydrogenic states. A new matrix is computed based on these eigenstates $\langle Wlm|z\Delta F + H_0|W'l'm'\rangle$ and diagonalized to find the next set of eigenstates. Off-diagonal elements associated with quantum states separated by energies greater than $(1+\delta)/n^3$ were considered insignificant and not computed. Off-diagonal elements could also be eliminated due to the nature of dipole interactions with the angular components of the wave functions. The oscillator strengths for p-s transitions were determined by a sum of p-s dipole transition amplitudes, weighted according to the field-free state composition of the individual Stark eigenstates. The computer algorithm was tested by generating the Stark spectrum of lithium and comparing with previously published Stark maps [3].

APPENDIX B: ASYMMETRIES FOUND IN FINITE QUANTUM REGIMES

The classical predictions include a slight asymmetry, particularly close to bifurcations due to the fact that uphill-oriented trajectories are classically more stable than their downhill counterparts. This effect is small compared to both the observed asymmetry in experimental argon recurrence maps and unexpectedly, computed hydrogen recurrence maps. The discrepancy with hydrogen computations is an artifact of a finite quantum system and is not directly accounted for in primitive COT.

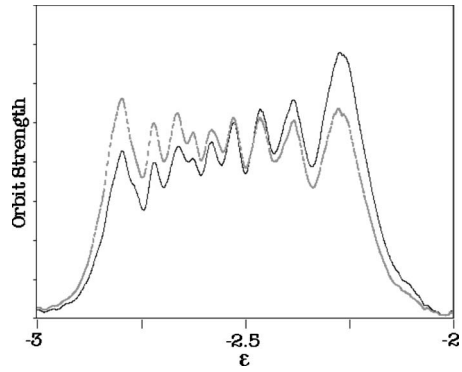

FIG. 8. The 8/9 orbit profile obtained from computed hydrogen Stark spectra in the $n=55-65$ range. The black line is a profile computed with true oscillator strength, the dotted, gray line is a profile computed with the true oscillator strengths xn^3.

Quantum mechanically the transition oscillator strength varies as n^{-3}. For a finite spectrum far from the continuum this is a source of asymmetry and produces orbit profiles artificially weighted to the uphill-oriented trajectories. This artifact can be easily corrected in computed spectra by eliminating the n^{-3} dependence when computing oscillator strengths. Experimental Stark spectra could be corrected by treating n as a continuous variable and simply weighting the signal strength by n^3. (This corrective procedure is only approximate because of n-manifold mixing.) In the limit of high n the oscillator strength differences between red and blue Stark states is negligible, leading to the expected symmetric distribution. Figure 8 shows the asymmetry artifact in the case of the 8/9 orbit profile obtained from computed Stark-spectra in the $n=55-65$ range.

APPENDIX C: SOLVING THE EQUATIONS OF MOTION IN SEMIPARABOLIC SPACE

With hyperbolic coordinates u and v defined with their corresponding momentum, the scaled Hamiltonian can be written and separated:

$$u = \sqrt{\tilde{r}+\tilde{z}}, \quad v = \sqrt{\tilde{r}-\tilde{z}}, \quad p_u = \tilde{p}_\rho v + \tilde{p}_z u, \quad p_v = \tilde{p}_\rho u - \tilde{p}_z v, \tag{C1}$$

$$\hat{H} = \frac{1}{2}\frac{p_u^2 + p_v^2 - 4}{u^2+v^2} + \frac{1}{2}(u^2 - v^2), \quad \text{separated}, \tag{C2}$$

$$\frac{1}{2}p_u^2 + \frac{1}{2}u^4 - \varepsilon u^2 - 1 = \beta, \quad \frac{1}{2}p_v^2 + \frac{1}{2}v^4 - \varepsilon v^2 - 1 = -\beta. \tag{C3}$$

Here β controls how the energy of the system is distributed between the u and v motions and can be directly related to the initial launching angle:

$$\beta = \cos(\theta_i). \tag{C4}$$

Inspection of the separated Hamiltonian yields potentials for the u and v coordinates:

$$V_u = \frac{1}{2}u^4 - \varepsilon u^2, \quad V_v = -\frac{1}{2}v^4 - \varepsilon v^2. \tag{C5}$$

Taking the derivative yields two separate force equations

$$F_u = -2u^3 + 2u\varepsilon, \quad F_v = 2v^3 + 2v\varepsilon. \tag{C6}$$

With a known launching angle and scaled energy these equations can be solved using Euler's method. The classical paths followed in semiparabolic space closely resemble Lissajou figures.

[1] M. L. Du and J. B. Delos, Phys. Rev. A **38**, 1896 (1988).
[2] U. Eichmann, K. Richter, D. Wintgen, and W. Sandner, Phys. Rev. Lett. **61**, 2438 (1988).
[3] J. Gao, J. B. Delos, and M. Baruch, Phys. Rev. A **46**, 1449 (1992).
[4] M. L. Keeler, H. Flores-Rueda, J. D. Wright, and T. J. Morgan, J. Phys. B **37**, 809 (2004).
[5] J. Gao and J. B. Delos, Phys. Rev. A **46**, 1455 (1992).
[6] M. L. Zimmerman, M. G. Littman, M. M. Kash, and D. Kleppner, Phys. Rev. A **20**, 2251 (1979).
[7] J. Gao and J. B. Delos, Phys. Rev. A **49**, 869 (1994).
[8] Michael Courtney, Neal Spellmeyer, Hong Jiao, and Daniel Kleppner, Phys. Rev. A **51**, 3604 (1995).
[9] M. L. Keeler, Heric Flores-Rueda, T. J. Morgan, and J. Shaw, Phys. Rev. A **69**, 012103 (2004).
[10] M. L. Keeler and T. J. Morgan, Phys. Rev. Lett. **80**, 5726 (1998).
[11] S. N. Pisharody, J. G. Zeibel, and R. R. Jones, Phys. Rev. A **61**, 063405 (2000).
[12] Michael Courtney, Hong Jiao, Neal Spellmeyer, and Daniel Kleppner, Phys. Rev. Lett. **73**, 1340 (1994).
[13] P. A. Dando, T. S. Monteiro, D. Delande, and K. T. Taylor, Phys. Rev. A **54**, 127 (1996).
[14] Annemieke Kips, Wim Vassen, and Wim Hogervorst, J. Phys. B **33**, 109 (2000).
[15] Annemieke Kips, Wim Vassen, Wim Hogervorst, and Paul A. Dando, Phys. Rev. A **58**, 3043 (1998).
[16] Bruno Hupper, Jorg Main, and Gunter Wunner, Phys. Rev. Lett. **74**, 2650 (1995).
[17] J. Gao and J. B. Delos, Phys. Rev. A **56**, 356 (1997).
[18] J. M. Mao, J. Shaw, and J. B. Delos, J. Stat. Phys. **68**, 51 (1992).
[19] Thomas F. Gallagher, *Rydberg Atoms* (Cambridge University Press, New York, 1994).